

# Characterizing the Three-Dimensional Organization of Telomeres

B. J. Vermolen,<sup>1\*</sup> Y. Garini,<sup>1</sup> S. Mai,<sup>2</sup> V. Mougey,<sup>4</sup> T. Fest,<sup>4,5</sup> T. C.-Y. Chuang,<sup>2,3</sup>  
A. Y.-C. Chuang,<sup>2</sup> L. Wark,<sup>2</sup> and I. T. Young<sup>1</sup>

<sup>1</sup>Delft University of Technology, Faculty of Applied Sciences, Department of Imaging Science and Technology, Delft, The Netherlands

<sup>2</sup>Manitoba Institute of Cell Biology, CancerCare Manitoba, University of Manitoba, Winnipeg, Manitoba, Canada

<sup>3</sup>Department of Otolaryngology Head and Neck Surgery, Health Sciences Centre, Winnipeg, Manitoba, Canada

<sup>4</sup>IETG Institut, University Hospital Jean Minjoz, Besançon, France

<sup>5</sup>Hematology-Immunology department, UPRES 3889, IFR GFAS, University Hospital Pontchaillou, Rennes, France

Received 12 November 2004; Revision Received 18 March 2005; Accepted 23 March 2005

**Background:** Quantitative analysis can be used in combination with fluorescence microscopy. Although the human eye is able to obtain good qualitative results, when analyzing the spatial organization of telomeres in interphase nuclei, there is a need for quantitative results based on image analysis.

**Methods:** We developed a tool for analyzing three-dimensional images of telomeres stained by fluorescence in situ hybridization in interphase nuclei with DNA counterstained with 4',6-diamidino-2-phenylindole. After deconvolution of the image, we segmented individual telomeres. From the location of the telomeres we derived a distribution parameter  $\rho_T$ , which indicated whether the telomeres were in a disk ( $\rho_T \gg 1$ ) or not ( $\rho_T \approx 1$ ). We sorted mouse lymphocyte nuclei and measured  $\rho_T$ . We also performed a bromodeoxyuridine synchronous cell sorting experiment on live cells and measured  $\rho_T$  at several instances.

**Results:** Measuring  $\rho_T$  for nuclei in G0/G1, S, and G2 produced  $1.4 \pm 0.1$ ,  $1.5 \pm 0.2$ , and  $14 \pm 2$ , respectively, showing a significant difference between G2 and G0/G1 or S. For the bromodeoxyuridine synchronous cell sorting experiment, we found a cell cycle dependency of  $\rho_T$  and a correlation between  $\rho_T$  and an observer.

**Conclusions:** In this study we present a quantitative method to characterize the organization of telomeres using three-dimensional imaging, image processing, and image analysis. © 2005 International Society for Analytical Cytology

**Key terms:** telomeres; three-dimensional imaging; image processing; fluorescence microscopy; fluorescence in situ hybridization

Mack Fulwyler was a pioneer in the introduction of modern technology for the analysis of cells and cellular constituents. His work was essential in turning qualitative descriptions in biology into quantitative ones. Further, he understood how it was possible to use these quantitative descriptions to study the dynamics of cellular processes. His interests were not limited to the use of fluorescence in flow cytometry; he realized how fluorescence digital imaging microscopy could provide the tools to answer many questions that were not approachable through fluorescence-activated cell sorting. He also saw how the combination of the two, flow cytometry and image cytometry, could provide an even more powerful mechanism for studying what we have come to know as system biology.

With the advent of sequence-specific DNA probes, the use of fluorescence microscopy in cancer and genetics research has steadily grown. Continuous improvements in fluorescence microscopic methods (hardware and software), specific labeling methods (wetware), and better understanding of the genome function and structure (bioinformatics) currently enable us to detect almost any

DNA sequence, gene, or chromosome region with high sensitivity and to address the central question: "What does it mean?"

Because fluorescence methods in most cases are based on digital imaging, quantitative analysis can be used and has become a crucial part of the methodologies. These

Contract grant sponsor: Delft Research Initiatives Information and Communication Technology; Contract grant sponsor: LifeTech; Contract grant sponsor: Life Science & Technology; Contract grant sponsor: Nano-electrophoresis, FOM; Contract grant number: 99TF13; Contract grant sponsor: MicroNed and Cyttron, Bsik; Contract grant sponsor: Canada Foundation for Innovation; Contract grant sponsor: Canadian Institutes of Health Research; Contract grant sponsor: CancerCare Manitoba; Contract grant sponsor: Fondation de France; Contract grant sponsor: Ligue Contre le Cancer du Doubs.

\*Correspondence to: B. J. Vermolen, Delft University of Technology, Faculty of Applied Sciences, Department of Imaging Science and Technology, Lorentzweg 1, 2628 CJ Delft, The Netherlands.  
E-mail: b.j.vermolen@tnw.tudelft.nl

Published online 12 September 2005 in Wiley InterScience (www.interscience.wiley.com).

DOI: 10.1002/cyto.a.20159

Table 1  
*Characteristics of Microscope System\**

FWHM <sub>lateral</sub>	200 nm
FWHM <sub>axial</sub>	400 nm
$\Delta x$	106 nm
$\Delta y$	106 nm
$\Delta z$	200 nm
M	63 $\times$
NA	1.4
Filters	DAPI, Cy3
Typical image size	200 $\times$ 200 $\times$ 100 pixels

\*FWHM, full width at half maximum; M, magnification; NA, numerical aperture.

methods, therefore, require suitable quantitative image analysis procedures and algorithms. As one of the last links in the chain, the algorithms being used must take into account the entire procedure that is being used, including the optical properties of the microscope and system, nature of the probes, and instrument parameters for the acquisition.

The organization of the interphase nucleus has been studied since the late 19th century (1). It is now well accepted that the position of chromosomes in the nucleus plays an important role in gene regulation (2). Recently, interest has also focused on telomeres whose importance to genomic stability was recognized as early as in the 1930s (3).

We have developed a method of studying the spatial organization of the genome in the three-dimensional (3D) interphase nucleus using flow sorted living cells. We analyze digital images of the 3D organization of the telomeres and how their positions change during the cell cycle. This method enables us to determine for the first time that telomere organization is cell cycle dependent with assembly of telomeres into a telomeric disk in G2 phase. Further, this disk formation is disrupted in tumor cells (4).

In this work we describe in more detail the algorithms that have been developed for the quantitative analysis of the telomeres in interphase nuclei. It can be extended to include centromeres and whole chromosomes.

## MATERIALS AND METHODS

### Cell Preparation

We studied two different cell nuclei populations based on mouse B lymphocytes. In the first case, immortalized mouse B lymphocyte cells were sorted according to their DNA content for the determination of G0/G1, S, or G2 phase. Cell cycle fractions were quantified through fluorescent-activated cell sorted analysis (4). Flow analyses were performed on an EPICS Altra cytometer operating under Multicycle software (Beckman-Coulter, Paris, France). Approximately 10 to 15 nuclei from each phase were analyzed for this study, representing a total of 35 cell nuclei.

To further study the phase transition timing along the cell cycle, we used the synchronous bromodeoxyuridine (BrdU) sorting method (4). The mouse B lymphocytes were labeled in vivo with BrdU. All BrdU-positive cells (i.e., cells in S phase, replicating their DNA) were live

sorted and placed into culture. Populations of nuclei were then harvested at different times (3, 3.5, 4.5, 5.5, 6.5, 7.5, 8, 8.5, and 9.5 h) of which approximately 20 nuclei were analyzed, representing a total of 180 cell nuclei.

For measurement of the telomeric disk, cells were first fixed and then telomere fluorescence in situ hybridization (FISH) was performed as describe previously (5) using a Cy3-labeled peptide nucleic acid (PNA) probe (DAKO, Glostrup, Denmark). 4',6-Diamidino-2-phenylindole (DAPI) was used as a DNA-specific counterstain. Telomere hybridizations were specific and we verified the correct number of telomeric signals observed at the ends of chromosomes prepared from primary cells using two-dimensional (2D) FISH metaphase spreads. The lymphocytes were fixed in such a way that the 3D structure of the nuclei was conserved (4).

### 3D Image Acquisition

For analysis of the telomere distribution, images were acquired with a Zeiss Axioplan 2 with a cooled AxioCam HR CCD in combination with a PlanApo 63 $\times$ 1.4 oil immersion objective (Zeiss). This gave a pixel (sampling) distance in the lateral plane of  $\Delta x = \Delta y = 106$  nm. The axial sampling distance between planes was  $\Delta z = 200$  nm. The point spread function (*psf*) of the objective, which determines the optical resolution, gave a full width at half maximum of approximately 200 nm in the lateral direction and 400 nm in the axial direction. Typical image size was 200  $\times$  200  $\times$  100 pixels. Table 1 shows a summary of these values for this imaging system.

Figure 1 illustrates the system resolution. An image of a pair of telomeres relatively far apart and an image of a pair close together are shown. It is clear that the telomeres at a distance of 1200 nm can be easily distinguished and telomeres at a distance of 400 nm are just barely separable.

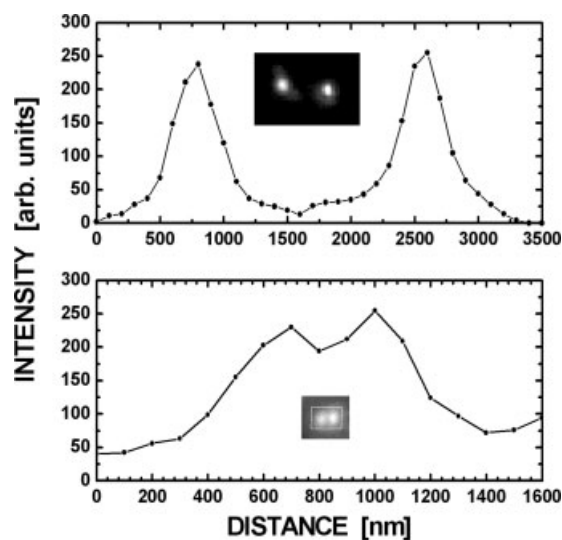


Fig. 1. Demonstration of the spatial resolution of our measurements. Two pairs of telomeres are shown: 1200 nm apart (top), which can be easily separated, and 400 nm apart (bottom). Inserts show the original image and graphs show the line section through the telomeres.

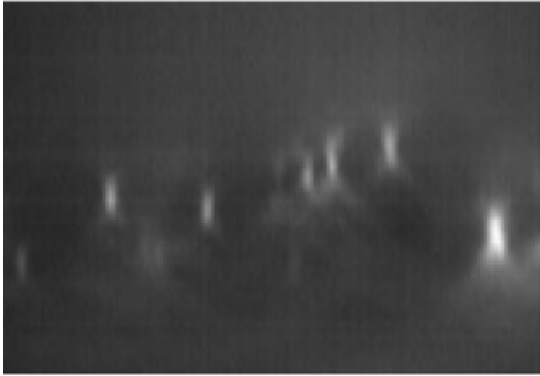
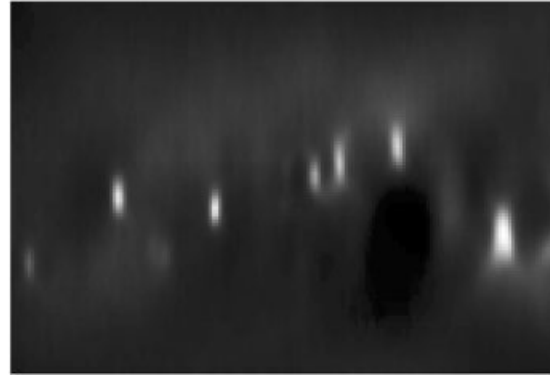
**Before deconvolution:****After deconvolution:**

Fig. 2. Demonstration of the effect of deconvolution. The left image is before deconvolution and the right after deconvolution. We clearly see that the left image has more blur and has less contrast than the right image. Both images are shown with a linear contrast stretch.

### 3D Image Processing

The 3D digital images were processed to improve the resolution by using constrained iterative maximum likelihood deconvolution (6), which is available in AxioVision 3.1 (Zeiss) software. This deconvolution method was chosen for this work because it has been shown to provide the best results (7). In this procedure we seek to find the most likely original image that could have produced the observed data. This devolves into minimizing a measurement between the recorded image and a blurred estimate of the object assuming (a) a certain model for the image noise (Poisson) and (b) separate estimates for the background and the *psf*. Poisson noise is an excellent model for the random variations found in fluorescent images acquired through high-quality CCD cameras. Our estimate for the *psf* was based on a theoretical calculation (8). In this specific case we work with the log-likelihood function  $\phi(\mathbf{f})$  which is given by:

$$\phi(\mathbf{f}) = \sum \mathbf{H}\mathbf{f} - \mathbf{g}^T \ln(\mathbf{H}\mathbf{f} + \mathbf{b}) + \gamma|\mathbf{f}|^2 \quad (1)$$

where  $\mathbf{g}$  is the digital fluorescence image that was recorded,  $\mathbf{b}$  is an estimate of the digital image background,  $\mathbf{H}$  is the *psf* of the imaging system,  $\gamma$  is a scalar “regularization” parameter that we are free to choose, and  $\mathbf{f}$  is the original image that we would like to estimate. Equation 1 is a concatenation of equations 4 and 5 in Vermeer et al. (7). The iterative algorithm seeks an image  $\mathbf{f}$  that minimizes  $\phi(\mathbf{f})$  and thereby produces the most likely  $\mathbf{f}$  that could have given rise to the measured  $\mathbf{g}$ .

Further, the deconvolution works with the constraint that the final restored image should consist of only non-negative numbers because we cannot have a negative number of photons. An example of the result of applying this procedure to telomere images is shown in Figure 2. After restoration, the image is interpolated in the axial ( $z$ ) direction from  $\Delta z$  to  $\Delta z'$  so that the sampling distance in all three directions is the same:  $\Delta z' = \Delta x = \Delta y = 106$  nm.

### 3D Image Segmentation and Analysis

Image segmentation and analysis of deconvolved 3D images of cells with labeled telomeres have been performed with a sequence of procedures that we have bundled together and named TeloView. The procedures themselves are from our image software library DIPIImage, which is available as public domain software (<http://www.qi.tnw.tudelft.nl/DIPIlib/>). The version of DIPIImage used in this development operates under MatLab (The MathWorks, Natick, MA, USA).

TeloView loads the 3D image and displays a maximum projection along the three main optical axes. Although thresholds and other parameters can be adjusted for display purposes, the analysis is performed on the original 3D data. After segmentation the 2D display indicates the location of the automatically found spots for verification. The user interface is shown in Figure 3.

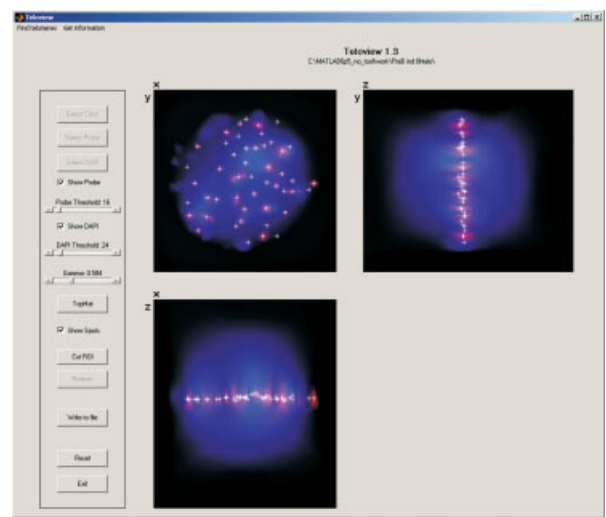


Fig. 3. Screenshot of the interface of TeloView. The screen shows three displays with maximum intensity projections along the three main axes. It also shows crosses at the locations where the software identified a telomere.

## Segmentation Algorithm

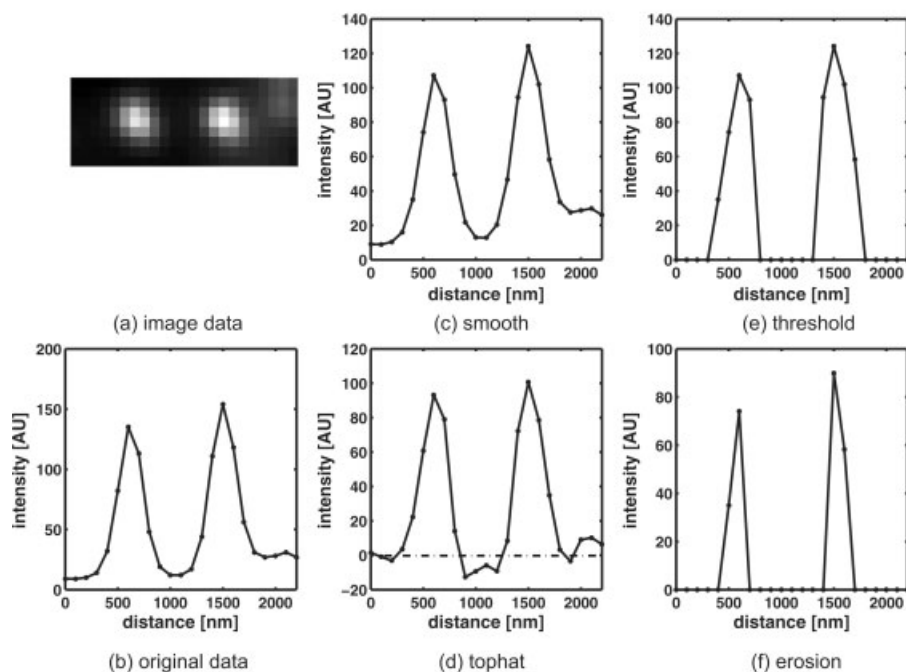


FIG. 4. Working of the algorithm. First we see the raw “image data.” A line through the center of this image gives a line section seen in “original data.” After we “smooth,” we perform a “TopHat” transform. Note that shading is now removed. We “threshold” and end up with two spots. One last “erosion” is performed to make sure that there are no remaining noise spikes.

### Segmentation

Before starting the segmentation we pre-process the data by smoothing with a 3D Gaussian kernel. Figure 4 shows how the data are transformed during the different steps of segmentation. For segmentation of the individual telomeres we have chosen an algorithm based on a morphologic TopHat transformation (9,10). The TopHat transform on an image  $A$  with structuring element  $B$  is defined as follows (11).

To find objects with high intensity (“light” objects):

$$\text{TopHat}(A, B) = A - \max_B(\min(A)) \quad (2)$$

To find objects with low intensity (“dark” objects):

$$\text{TopHat}(A, B) = \min_B(\max(A)) - A \quad (3)$$

The “structuring element,”  $B$ , can be a quite general 3D gray-value object, but in our case we have chosen for the simple case that  $B$  is spherical.  $B$  should be larger than the objects that are being sought but smaller than any shading in the background. For a gray-scale image of telomeres, the telomeres would be our objects and any nonspecific binding of Cy3 uniform spread over the nucleus gives us shading. Thus, for our case, this translates to a spherical  $B$  with radius 742 nm (7 pixels).

After the TopHat transform, the resulting image is thresholded with a user-chosen value to produce a binary mask. To eliminate noise spikes that may remain, we conclude with an erosion. This algorithm gives satisfying results for small telomeres. Using the binary image mask from the segmentation, the center of gravity of each dot is

found. This gives coordinates  $(x_i, y_i, z_i)$  for each individual dot, where  $i$  is the index number of the dot.

### Analysis

Observing the organization of telomeres in many cells, we see that the envelope shape of the telomeres is usually a spheroid, as illustrated in Figure 5. A spheroid is a geo-

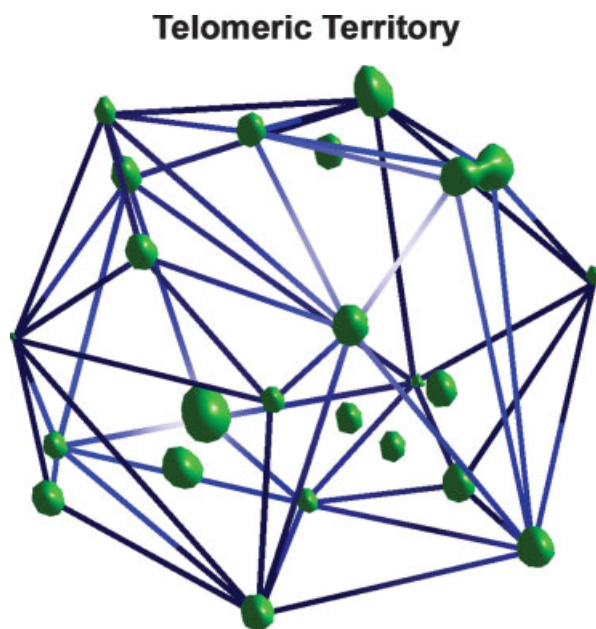


FIG. 5. The telomeric territory can be given by a convex body containing all the telomeres. In most cases this envelope can be approximated by a geometric figure called a spheroid.

## Oblate Spheroid

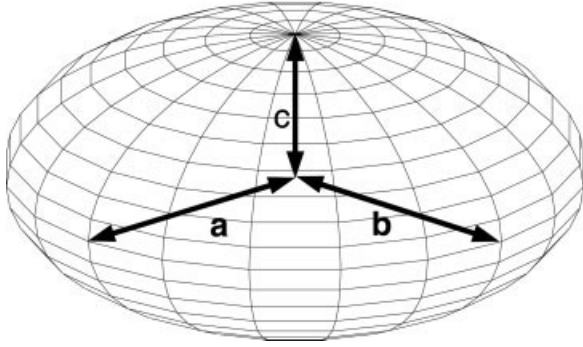


FIG. 6. The telomeric territory is characterized as an oblate spheroid, where two of the main axes,  $a$  and  $b$ , are of equal length and the third main axis,  $c$ , is shorter. The ratio  $\rho_T = a/c$  now gives a measure of the flatness of the spheroid.

metric figure, like an ellipsoid, where the two main axes,  $a$  and  $b$ , are equal, and the third axis  $c$  has a different length,  $c$ . This is shown in Figure 6. If  $a = c$ , we have a sphere; if  $a < c$ , we have a prolate spheroid; and if  $a > c$ , we have an oblate spheroid. We can therefore define a telomere ratio parameter,  $\rho_T$ , which gives us a measurement of the disk-like nature of this organization. If  $\rho_T \approx 1$ , then the telomeres are distributed in a spherical way within the cell. However, if  $\rho_T > 1$ , then the telomeric territory is more disk-like. In the following, we describe how we determine  $\rho_T$ .

Given the spatial coordinates of every spot ( $x_i, y_i, z_i \mid i = 1, 2, \dots, N$ ), we rotate the original spatial coordinates ( $x, y, z$ ) to a new orthogonal coordinate system such that the distance from the spots to the new axes is minimized. This procedure is known as a principal component analysis (12). To accomplish this, we calculate the singular values (eigenvalues) of the covariance matrix of the data points. The three singular values,  $\lambda_1 \geq \lambda_2 \geq \lambda_3$ , are real and positive and can be ordered. They are the variances of the distances from the spots to the new principal axes. The standard deviation for each new axis is then given by:

$$\sigma_i = \sqrt{\lambda_i} \quad (4)$$

From these standard deviations, we then define  $\rho_T$  as:

$$\rho_T = \frac{\sqrt{\sigma_1 \sigma_2}}{\sigma_3} \quad (5)$$

Given that we work with ordered  $\lambda$ s, we have:

$$\rho_T \geq 1 \quad (6)$$

## RESULTS

Results of the analysis of the cell-sorted mouse lymphocytes are presented in Table 2. Here we see small values (close to 1) of  $\rho_T$  for nuclei in G0/G1 and S phases, which indicate that telomeres are distributed throughout the

Table 2  
Results of Phase-Sorted Cells

Phase	$\rho_T$
G0/G1	$1.4 \pm 0.1$
S	$1.5 \pm 0.2$
G2	$14 \pm 2$

cell. For the telomeres in G2, however, there is a high value of  $\rho_T$ , indicating that the telomeres form a disk. A statistical analysis, using a two-sample Student's  $t$  test with unequal variances, indicates a significant difference in  $\rho_T$  between G0/G1 and G2 phases ( $P < 0.01$ ) and between S and G2 phases ( $P < 0.01$ ). An example of typical distributions of telomeres in lymphocytes is shown in Figure 7.

The results of the BrdU synchronization experiment can be seen in Figure 8. In the left graph we see the results of nuclei counted by a human observer. The observer was presented with a 2D computer display of the 3D distribution. A display of the DAPI counterstain indicated the position of the total DNA.

The nuclei are divided into three groups: (a) nuclei with telomeres in a disk, (b) nuclei in mitosis, and (c) other nuclei (interphase nuclei without a telomeric disk). At 3.5 h, 90% of nuclei show a telomeric disk. Based on timing since S phase, most nuclei are believed to be in late G2. After this point, cells continue through the cell cycle, enter into prometaphase and metaphase (i.e., mitosis), and the number of cells in G2, accordingly, decreases. This correlates with the observation that the fraction of cells with a telomeric disk decreases and the number of cells going into mitosis increases.

In the right graph of Figure 8 we show the result of  $\rho_T$  calculations on the same population of nuclei. We also

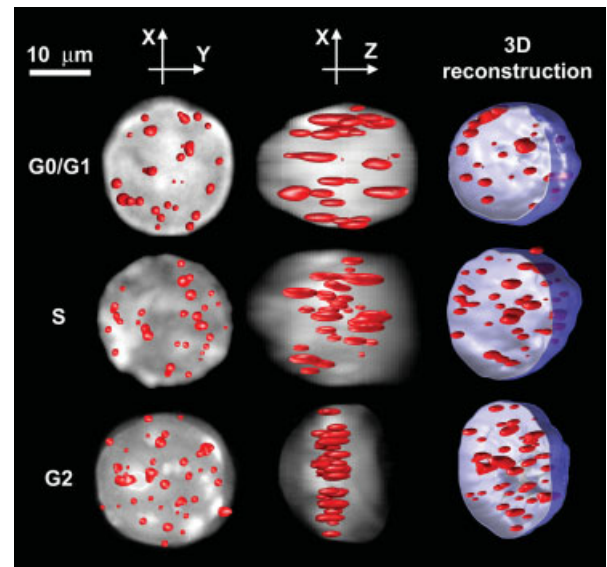
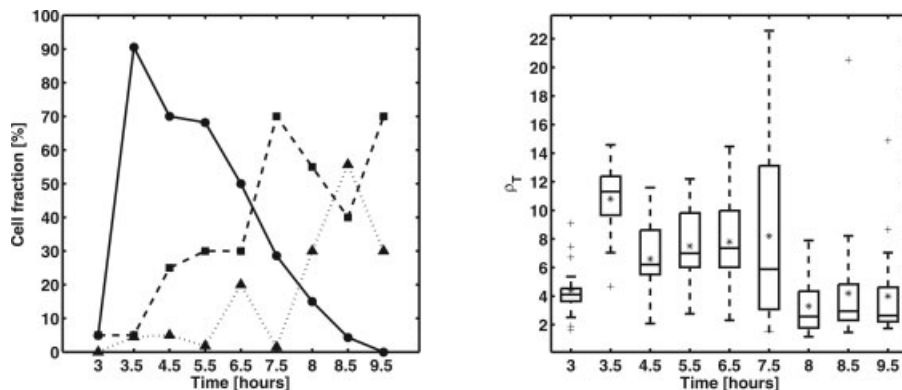


FIG. 7. Three typical distributions of telomeres. A nucleus is seen in G0/G1 phase (top), S phase (middle), and G2 phase (bottom). Every nucleus is shown in top view ( $xy$  plane), in side view ( $xz$  plane), and as a 3D visualization. We clearly see that the telomeres in G0/G1 and S phases are distributed throughout the nucleus, whereas those in G2 phase line up into a disk.

FIG. 8. Results of synchronous BrdU sorting experiment. In the left graph we show the results obtained by a human observer. For each time point approximately 20 nuclei were analyzed and sorted into 3 categories: nuclei with a telomeric disk (black line with circles), nuclei in mitosis (dashed line with squares), and nuclei in interphase without a telomeric disk (dotted line with triangles). In the right graph we show a box plot of  $\rho_T$  calculations on the same population. Asterisks indicate the mean  $\rho_T$  at every time point and boxes and whiskers represent the 0th, 25th, 50th, 75th, and 100th percentiles of the measurement. Plus signs denote outliers.



observe that the *spread* of  $\rho_T$  increases and reaches a maximum at 7.5 h. This coincides with the left graph, where we see an increase in the number of cells without a telomeric disk relative to the number with a telomeric disk. The right graph, however, does not correspond exactly to the left graph calculated by the observer because it calculates the average  $\rho_T$  value of the complete population of nuclei at that time point; the nuclei can be in different cell phases. By using a threshold on the  $\rho_T$  value, it is possible to imitate the classification of nuclei in a disk. If we choose a threshold of 6.7 between nuclei in a disk ( $\rho_T > 6.7$ ) and others, we can calculate the fraction of these nuclei and get approximately the same curve as the human observer got. Apparently this is the subjective threshold that was selected when the left graph of Figure 8 was created.

In Figure 8 we notice that the fraction of cells in mitosis at 7.5 h is twice as high as those with a disk. In Figure 9 we see the histogram of the data at 7.5 h, which suggests two populations with twice the amount of low  $\rho_T$  cells compared with high  $\rho_T$  cells. In the box plot in Figure 8, we also see outliers that are easily explained if the data within the box and whiskers are from the population with low  $\rho_T$  and the outliers are from the population with high  $\rho_T$ . The outliers in Figure 8 at  $t = 8.5$  h, for example, are due to the last few cells from the G2 population that have not yet entered mitosis.

## DISCUSSION

For the first time we show that the telomere organization in the nucleus can be characterized and is cell cycle dependent. It is very important to recognize the need for 3D image processing for quantification where objective measurements are preferable above the subjective view of an individual. We have developed an objective means to quantify and analyze the spatial arrangement of telomeres, a task that is, essentially, too difficult for ordinary human vision that can only do qualitative estimates. This is done by calculating a parameter,  $\rho_T$ , whose value measures the disk-like compactness of the telomere distribution. We show that  $\rho_T$  is significantly higher in cells in G2 than in G0/G1 or S, which suggests that the telomeres form a disk during G2. This is also observed in a synchronous BrdU sorted population, where high  $\rho_T$  values are observed after

3.5 h and where the disk phenomenon decreases as cells leave G2. Although a human observer can only threshold the data into fractions called “disk” or “no disk” with a subjective threshold, our method allows this threshold, but we can distill more information out of the data like the distribution of the  $\rho_T$  values. It may be valuable in the future to combine these data with the DAPI intensity distribution that may allow distinguishing nuclei in mitosis (based on intensity uniformity) from the other cell cycle phases.

These findings shed new light on the cell cycle mechanism. It remains to be determined whether the telomeric disk is a precursor structure that will later position the chromosomes into the equatorial disk.

Nevertheless, we have already observed that, in cancer cells, the telomeres tend to form aggregates (4), which is another indication to the large role that the organization of the genome in the nucleus has in cancer development.

We are developing methods to quantify the size of a telomere or telomere aggregates, where telomeres are found in close association, as previously shown (4). It is therefore important to quantify such aggregates and test their correlation with cancer progress. Aggregates are usually significantly larger than individual telomeres. As a result, our current algorithm tends to miss these spots because

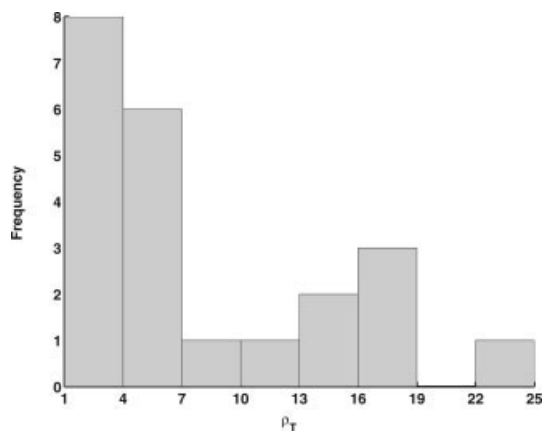


FIG. 9. Histogram of measured  $\rho_T$  at 7.5 h after BrdU pulse labeling. The histogram suggests two populations: one with low  $\rho_T$  and one with high  $\rho_T$ .

the TopHat transform is sensitive to the size of the telomeres. Therefore, we are currently working on an improved segmentation procedure based on a scale-space algorithm (13) that looks most promising. Another suggested path of research is to follow telomeres through the entire cell cycle in living cells.

#### ACKNOWLEDGMENTS

T. C.-Y. Chuang and A. Y.-C. Chuang were supported through a Canadian Institutes of Health Research Strategic Training Program, "Innovative Technologies in Multidisciplinary Health Research Training" fellowship. V. Mougey and T. Fest were supported by Fondation de France and Ligue Contre le Cancer du Doubs.

#### LITERATURE CITED

1. Rabl C. Über Zellteilung. In: Gegenbauer C, editor. *Morphologisches Jahrbuch*. Volume 10. 1885. p 214-330.
2. Marshall WF. Order and disorder in the nucleus. *Curr Biol* 200;12: R185-R192, Wilhelm Engelmann, Leipzig.
3. McClintock B. The stability of broken ends of chromosomes in Zea mays. *Genetics* 1941;26:234-282.
4. Chuang TCY, Moshir S, Garini Y, Chuang AY-C, Young IT, Vermolen B, Doel Rvd, Mougey V, Perrin M, Braun M, et al. The three-dimensional organization of telomeres in the nucleus of mammalian cells. *BMC Biol* 2004;2(12).
5. Figueroa R, Lindenmaier H, Hergenbahn M, Nielsen KV, Boukamp P. Telomeres erosion varies during in vitro aging of normal human fibroblasts from young and adult donors. *Cancer Res* 2000;60:2770-2774.
6. Schaefer LH, Schuster D, Herz H. Generalized approach for accelerated maximum likelihood based image restoration applied to three-dimensional fluorescence microscopy. *J Microsc* 2001;204:99-107.
7. Verveer PJ, Gemkow MJ, Jovin TM. A comparison of image restoration approaches applied to three-dimensional confocal and wide-field fluorescence microscopy. *J Microsc* 1999;193:50-61.
8. Gibson SF, Lanni F. Experimental test of an analytical model of aberration in an oil-immersion objective lens used in three dimensional light microscopy. *J Opt Soc Am* 1991;8:1601-1613.
9. Meyer F, Beucher S. Morphological segmentation. *J Vis Commun Image Represent* 1990;1:21-46.
10. Meyer F. Iterative image transformations for an automatic screening of cervical smears. *J Histochem Cytochem* 1979;27:128-135.
11. Young IT, Gerbrands JJ, van Vliet LJ. *Fundamentals of Image Processing*. In: Madisetti VK, Williams DB, editors. *The digital signal processing handbook*. Boca Raton: CRC Press/IEEE Press; 1998. p 51.1-51.81.
12. Wall ME, Rechtsteiner A, Rocha LM. Singular value decomposition and principal component analysis. In: Berrar DP, Dubitzky W, Granzow M, editors. *A practical approach to microarray data analysis*. Norwell: Kluwer; 2003. p 91-109.
13. Olivo-Marin J-C. Extraction of spots in biological images using multiscale products. *Pattern Recogn* 2002;35:1989-1996.